Microstructure evolution in the hypo-eutectic alloy $Al_{0.75}CrFeNi_{2.1}$ manufactured by laser powder bed fusion and subsequent annealing

U. Hecht[1], A. Vayyala[2,3], P. Barriobero-Vila[4,5], N. Navaeilavasani[1], S.Gein[1], I. Cazic[1], J. Mayer[2,3]

[1]Access e.V., Aachen, Germany

[2]Central Facility for Electron Microscopy (GFE), RWTH Aachen University, Germany

[3]Ernst Ruska-Centre for Microscopy and Spectroscopy with Electrons, Forschungszentrum Jülich GmbH, Jülich, Germany

[4]German Aerospace Center (DLR), Institute of Materials Research, Cologne, Germany

[5]Technical University of Catalonia (UPC), Department of Materials Science and Engineering, 08019 Barcelona, Spain

*Corresponding author: u.hecht@access-technology.de

Abstract

The hypo-eutectic medium entropy alloy $Al_{0.75}CrFeNi_{2.1}$ was processed by laser powder bed fusion (LPBF). The off-equilibrium solidification conditions prohibited coupled eutectic growth. Instead, the primary face centered cubic phase A1(FCC) solidified with a cellular morphology and the body centered, initially ordered B2(BCC) phase formed as a thin intercellular envelope. During post-build annealing an ultrafine quasi-lamellar pattern evolved following BCC growth and coarsening. The novel solid state transformation from cellular to lamellar morphology was attributed to a pronounced anisotropy of the FCC|BCC phase boundary energy. Microstructure evolution was also studied during continuous heating using in situ high-energy synchrotron X-ray diffraction (HEXRD) carried out at the beamline P07-HEMS of PETRA III (German Electron Synchrotron, DESY). The ultrafine and nano-scale features of the microstructure were quantitatively analyzed by atom probe tomography (APT) in the as-built condition and after isothermal annealing at 950°C. The benefits of LPBF processing were discussed on the basis of mechanical properties measured by 3-point bending. The estimated tensile properties after annealing at 950°C / 6h reached YS ≈ 860 MPa, UTS ≈ 1384 MPa with an elongation at fracture of ≈11%. Tensile properties in the as-built condition were comparable to martensitic steels.

Keywords Additive manufacturing, eutectic high entropy alloys, microstructure, atom probe tomography, synchrotron X-ray diffraction

1. Introduction

From the many eutectic alloy systems, only few have led to well established material families for structural applications. These include Fe-C cast irons [1] and Al-Si based alloys [2]. Other eutectics have excelled as solder alloys and liquid metal alloys mainly due to their low melting temperature. None the less, materials research has always continued to look at eutectics for structural applications. The major developments from over 5 decades of research are presented in a recent review paper [3], which also includes eutectic high entropy alloys (EHEA). Among these, eutectics with lamellar microstructure composed of (A1)FCC and (B2)BCC show very promising properties. They are potentially capable of operating at elevated temperature and filling the gap between steels and Ni-base alloys.

Such eutectics have been reported in ternary Al-Ni-Fe, quaternary Al-Ni-Fe-Cr and quinary Al-Ni-Fe-Cr-Co alloys, as outlined in [4]. In the ternary system Al-Ni-Fe, a eutectic alloy with composition $Ni_{50}Fe_{30}Al_{20}$ [5] was investigated after slow directional solidification and showed room-temperature tensile yield strength of 575 MPa, elongation at fracture of 12% and fracture toughness of 30.4 MPa$\sqrt{m}$. In the quaternary system Al-Ni-Fe-Cr, a eutectic alloy with composition near $Ni_{44}Fe_{20}Cr_{20}Al_{16}$ [6] was investigated in the as-cast state and reached room-temperature tensile yield strength of 479 MPa and an elongation at fracture of 12.7%. In the quinary system Al-Ni-Fe-Cr-Co, a eutectic alloy near $Ni_{34.4}Fe_{16.4}Co_{16.4}Cr_{16.4}Al_{16.4}$ was investigated in great detail [7, 8, 9]. Its room-temperature tensile yield strength reaches about 550 MPa with elongation at fracture of about 16%. Recent investigations of this alloy [10, 11, 12] focused on microstructure evolution and mechanical properties after heavy cold-rolling and subsequent annealing treatments. The yield strength increase associated to the ultrafine recrystallization structure is remarkable and depends on the recrystallized fraction [10]. Values around 1200 MPa are reported for the fully recrystallized condition after annealing at 800°C, with elongations at fracture of around 12% [11].

The most recent publications refer to additive manufacturing by laser metal deposition [13,14] and laser powder bed fusion [15, 16], the alloys at case being $AlCo_{0.2}CrFeNi_{2.1}$ and $AlCoCrFeNi_{2.1}$, respectively. For the as-built condition, outstanding properties are reported associated to an ultrafine [15] and even nano-scale [16] structure with a high dislocation density inherited from the LPBF process. During short duration annealing treatments [16] the micro-scale residual stress is effectively reduced, while the nano-lamellar structure and excellent materials strength is retained.

Our own research focused on laser powder bed fusion (LPBF) of a Co-free alloy with slightly off-eutectic composition close to $Al_{0.75}CrFeNi_{2.1}$ aiming at an application-oriented, resource-efficient and sustainable material development strategy. We selected the hypo-eutectic alloy composition with an aluminum content of about 15.4 at. % in order to safely avoid the formation of primary (B2)BCC phase. This ordered phase requires high energy to activate the slip systems and is therefore sensitive to cracking in response to the thermo-mechanical stresses arising in the LPBF process conditions. The alloy composition was thus Al15.4-Cr19.6-Fe20.9-Ni44.1 (at. %). This paper presents the major experimental observations and results as follows: *Section 2* describes the experimental methods applied in this study. *Section 3.1* presents the processing conditions using LPBF and post-build annealing treatments, with emphasis on the microstructure and also including preliminary mechanical properties. *Section 3.2* presents the results obtained from *in situ* high-energy X-ray diffraction (HEXRD) measurements carried out at the Deutsches Elektronen-Synchrotron DESY. They provide the phase evolution during continuous heating of an LPBF specimen up to 1200°C. S*ection 3.3* presents the nano-scale features of the microstructure based on atom probe tomography (APT) for an as-built and an annealed specimen. *Section 4* contains a comprehensive discussion of the results and presents novel insights gained throughout this research. *Section 5* presents the main conclusions and briefly outlines future research directions. Throughout the text, whenever necessary, the Strukturbericht designations A1, A2 and B2 are used along with FCC (face centered cubic) and BCC (body centered cubic) to clearly distinguish the phases in the microstructure. FCC and BCC are used if the distinction is not absolutely necessary. BCC then means the sum of (B2)BCC and A2(BCC).

2. Experimental Methods

2.1 Sample manufacturing by laser powder bed fusion (LPBF) and subsequent annealing

Alloy powder production using the VIGA process (Vacuum induction melting Inert Gas Atomization) was commissioned to Rosswag GmbH. The provided powder with a particle size distribution ranging from 10 to 90 µm displayed a median value of d_{50}=27 µm. The chemical composition of the powder was analyzed by inductively coupled plasma mass spectrometry (ICP), while the nonmetallic impurities were analyzed by inert gas fusion (LECO-IGF) and combustion and infrared absorption (LECO-CS), respectively.

Laser powder bed fusion (LPBF) was performed in an Aconity Mini system, equipped with a single mode Yb fiber laser with up to 400W power and an optional baseplate preheating system. A range of process parameters, specifically laser power (P), laser scanning velocity (v) and hatching distance (ΔX) were screened systematically in several build jobs encompassing 10x10x10 mm cube specimens. The laser beam diameter (d) as well as the powder layer thickness (Δz) were kept constant at 80 µm and 40 µm, respectively. Bidirectional hatching was used in all cases, along with a 90° rotation of scan vectors in each consecutive layer. The highest specimen density was obtained for P ranging from 200 to 250 W and v ranging from 1000 to 1200 mm/s. Baseplate preheating to 200°C was successful to avoid delamination of the first layers. Rectangular samples of 30x10x10 mm were built with chessboard hatching and used to machine test specimens for three-point bending experiments. The LPBF samples were further subjected to annealing heat treatments in a Nabertherm tube furnace under Argon atmosphere at 850°C for 6 hours and 950°C for 6 hours, respectively, followed by water quenching. The heat treatments aimed at enabling microstructure evolution towards thermodynamic equilibrium while also relaxing residual stresses inherited from the LPBF build process.

The microstructure of as-built and annealed LPBF specimens was investigated by scanning electron microscopy using an SEM type ZEISS Ultra 55 and backscatter electron imaging (BSE) for enhanced phase contrast (atomic number or Z-contrast). A micro-indentation device (Anton Paar MHT^3) was used to characterize the material in the as-built and annealed conditions using a Vickers indenter. Furthermore, 3-point bending was used to determine the materials flexural

properties using small rectangular specimens with dimensions 30x5x1.6 mm and a miniature test stage type MTI-5000 EBSD. The experimental analysis of microstructure formation was complemented with thermodynamic computations of phase equilibria using the software Thermo-Calc and the commercially available database TCHEA2 from Thermo-Calc AB, https://thermocalc.com/.

2.2 In-situ high-energy synchrotron X-ray diffraction

In situ high-energy synchrotron X-ray diffraction (HEXRD) was carried out at the beamline P07-HEMS of PETRA III (German Electron Synchrotron, DESY) [17]. The experimental parameters used are: beam energy = 100 keV; wavelength = 0.124 Å; image-acquisition time = 6 s; sample-detector distance= 1602.4 mm; and slit-aperture size= 0.8 × 0.8 mm^2. Continuous heating of a cylindrical sample with diameter 4 mm and length 10 mm was performed in vacuum from room temperature (RT) up to 1200 °C at 20 °C/min in a modified dilatometer Bähr 805A/D equipped with an induction furnace [18]. The sample was kept fixed during acquisition. The temperature was monitored by a thermocouple welded next to the incoming beam, positioned at the centre of the sample. Diffraction images of entire Debye–Scherrer rings from the bulk alloy were recorded in transmission mode (thickness = 4 mm) using an image-plate detector Perkin Elmer XRD 1621.

The qualitative analysis of the phase evolution during continuous heating consisted of: a) the conversion of Debye-Scherrer rings into Cartesian coordinates (azimuthal angle, 2-Theta) and the subsequent projection on the 2-Theta axis of the sum intensity of their Bragg reflections, and b) Azimuthal integration along the Debye-Scherrer rings using the software Fiji [19] and Fit2d [20], respectively. Quantitative phase analysis providing the evolution of volume fraction of phases was performed by the Rietveld method using the software Maud [21]. A LaB_6 powder standard was used to obtain the instrumental parameters of the setup.

2.3 Microstructure characterization by atom probe tomography (APT)

For the investigations by atom probe tomography (APT), specimens from various locations in the microstructure were prepared using a Helios Nanolab 650i dual beam focused ion beam (FIB) (Thermo Fisher Scientific, USA) tool. The APT analysis was carried out using a LEAP4000X HR instrument (Ametek Inc.) operating in laser mode with laser pulse energies of 30 pJ, pulse frequency of 250 kHz and detection rate of 0.01 ions per pulse. The base specimen temperature for all the measurements was maintained at 50 K. APT data reconstruction and analysis was performed using the Integrated Visualization and Analysis Software (IVAS) package 3.6.14 (Ametek Inc.). A careful determination of reconstruction parameters and deconvolution of peak overlaps in mass spectra were performed for accurate compositional analysis.

3. Results

3.1 Laser powder bed fusion and subsequent annealing of alloy $Al_{0.75}CrFeNi_{2.1}$

High quality samples were obtained by LPBF using the alloy powder atomized by VIGA (Vacuum induction melting Inert Gas Atomization). The optimum process parameters *P*-laser power and *v*-scanning velocity were obtained after a small screening series, during which the laser beam diameter (*d*), the powder layer thickness (Δz) and the hatch spacing (Δx) were kept constant. A bidirectional hatching strategy with 90° rotation of scan vectors in each consecutive layer was applied. *Table 1* summarizes the optimized process parameters for a baseplate preheating temperature of 200°C. *Table 2* provides the alloy composition as measured by chemical analysis of the as received powder, here including the nonmetallic impurities O, N, C, H. The measured alloy composition is close to the nominal $Al_{0.75}CrFeNi_{2.1}$ composition ($Al_{15.4}Cr_{20.6}Fe_{20.6}Ni_{43.3}$) with slightly higher Ni and Fe at the expense of Cr (compare *Table 2*). The deviations are considered acceptable for the experimental investigation at case. *Table 2* also lists the composition of the eutectic alloy which according to Jin et al. [6] is close to $Al_{0.8}CrFeNi_{2.2}$, while thermodynamic computations with the database TCHEA2 predict it close to $Al_{0.8}CrFeNi_{2.1}$.

Figure1 presents an overview of the powder morphology (*Figure 1a*) and displays an as-built cube of size 10x10x10 mm (*Figure 1b*). Furthermore, *Figure 1c* and *Figure 1d* show the representative

microstructure in build direction before and after applying an annealing heat treatment (950°C/6h/water quenching). Melt pool boundaries are highlighted by a white dotted line. The main observation refers to the difference between the as-built and the annealed microstructure: the multiphase microstructure expected in the hypoeutectic alloy develops during annealing rather than solidification. The as-built microstructure is obviously the result of a strongly out of equilibrium solidification process.

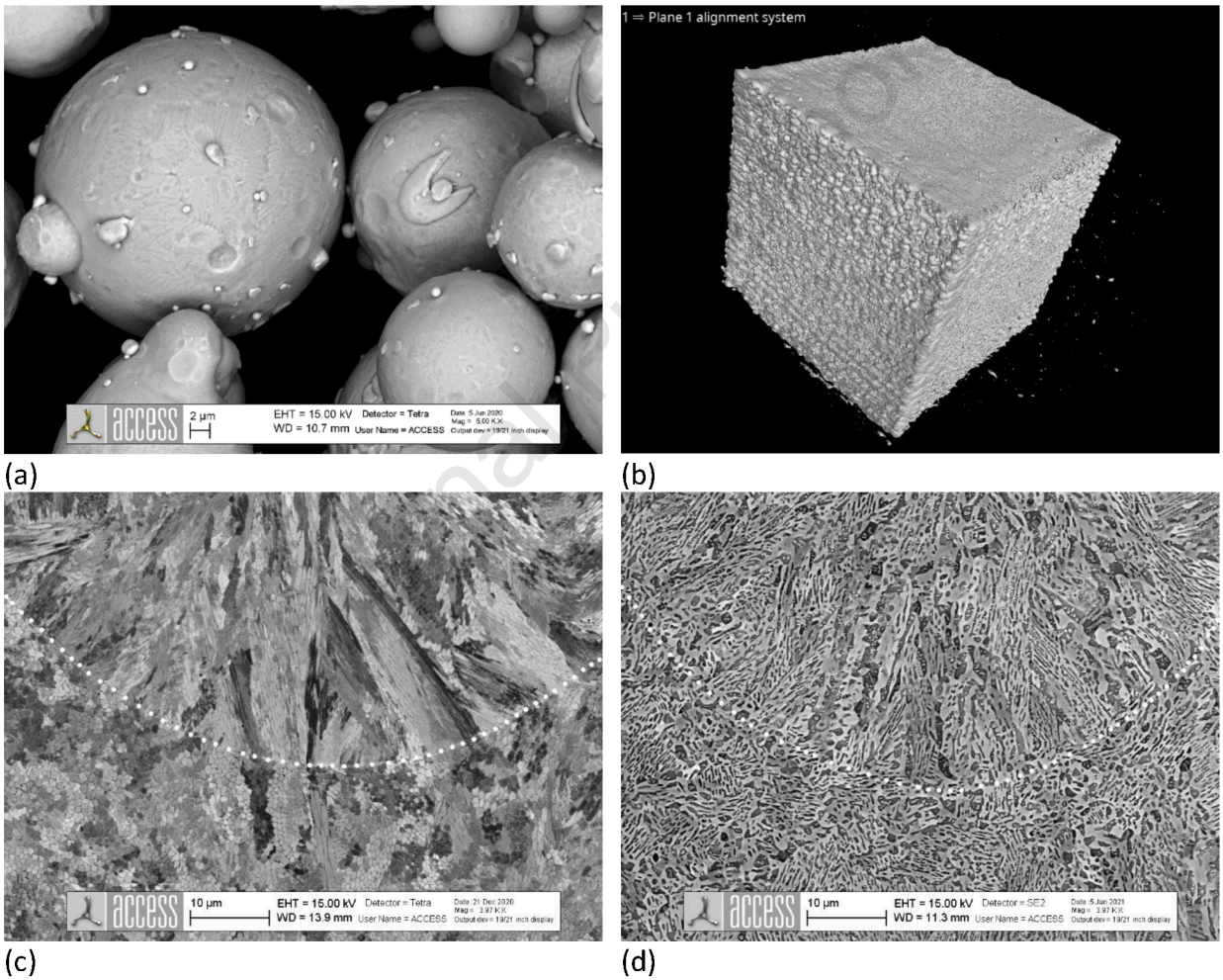

Figure 1: (a) SEM image of powder particles from alloy Al0.75CrFeNi2.1, (b) scan image of an as-built sample used to optimize the build parameters, along with SEM-BSE images of the microstructure in build direction (c) before and (d) after an annealing heat treatment at 950°C / 6h. The white dotted line is highlighting a melt pool boundary.

Table 1: LPBF processing parameters for dense samples (density >99.8%).

Preheating (°C)	Laser power (W)	Scanning velocity (mm/s)	Hatch spacing (µm)	Layer thickness (µm)
200°C	200-250	1000-1200	80	40

Table 2: Experimental composition of the hypoeutectic alloy (powder) by chemical analysis using ICP, LECO-IGR and LECO-CS compared to the nominal composition and the eutectic composition.

	Alloying elements (at.%)				Impurities by LECO-IGF, -CS (ppm)			
	Al	Cr	Fe	Ni	O	N	C	H
Experimental	15.4	19.6	20.9	44.1	150	30	81	6
Nominal	15.5	20.6	20.6	43.3	Not specified			
$Al_{0.8}CrFeNi_{2.2}$ [(a)]	16.0	20.0	20.0	44.0	Not specified			
$Al_{0.8}CrFeNi_{2.1}$ [(b)]	16.3	20.4	20.4	42.8	Not specified			

[(a)] eutectic composition by [6]; [(b)] eutectic composition calculated by Thermo-Calc and TCHEA2

Figure 2 displays a detailed view of the microstructure in section planes perpendicular to the build direction. In the as-built condition (*Figure 2a*) an ultrafine cellular morphology of the A1(FCC) phase is observed, the cells being enveloped by a dark BCC phase. At the nano-scale the BCC phase is spinodally decomposed into an ordered B2(BCC) and a disordered A2(BCC) phase (see section 3.3). Cellular spacings were evaluated by Delaunay triangulation using Fiji software [18] giving a median value of 0.52 µm. This cellular structure is the result of strongly out of equilibrium solidification conditions pertaining to LPBF. Some features observed for single phase FCC alloys [22] can be identified, like the considerable disorder in the cellular array and a rather wide range of spacings.

During post-build isothermal annealing treatments the metastable LPBF microstructure evolves towards thermodynamic equilibrium (*Figure 2b* through *Figure 2d*) along a unique solid state transformation pathway, which involves growth of the BCC phases and anisotropic coarsening. The cellular pattern vanishes, being replaced by a quasi-lamellar pattern. The early stages of growth and coarsening were captured upon annealing at 750°C and are highlighted in *Figure 2b*. The figure shows merging of neighboring cells, thereby eventually enclosing BCC islands. Gradually and due to pronounced anisotropy of the A1(FCC)|B2(BCC) phase boundary energy the microstructure develops a lamellar character. Inside B2(BCC) lamellae the A2(BCC) phase appears as dispersed particles following coarsening of the initially nano-fine spinodal mixture.

The (A2)BCC particles are mostly attached to the A1(FCC) phase, which is mainly due to the narrow space available for coarsening. An estimate of the spacing, i.e. the distance between neighboring (A1)FCC lamellae gives 430 nm after annealing at 850°C / 6h and 670 nm after annealing at 950°C / 6h. During annealing the (A1)FCC phase develops clearly visible subgrain boundaries (*Figure 2d*), a sign of the originally high dislocation density (crystalline misorientation) peculiar for LPBF processing, compare [23]. *Table 3* summarizes the key microstructure characteristics obtained from image analysis.

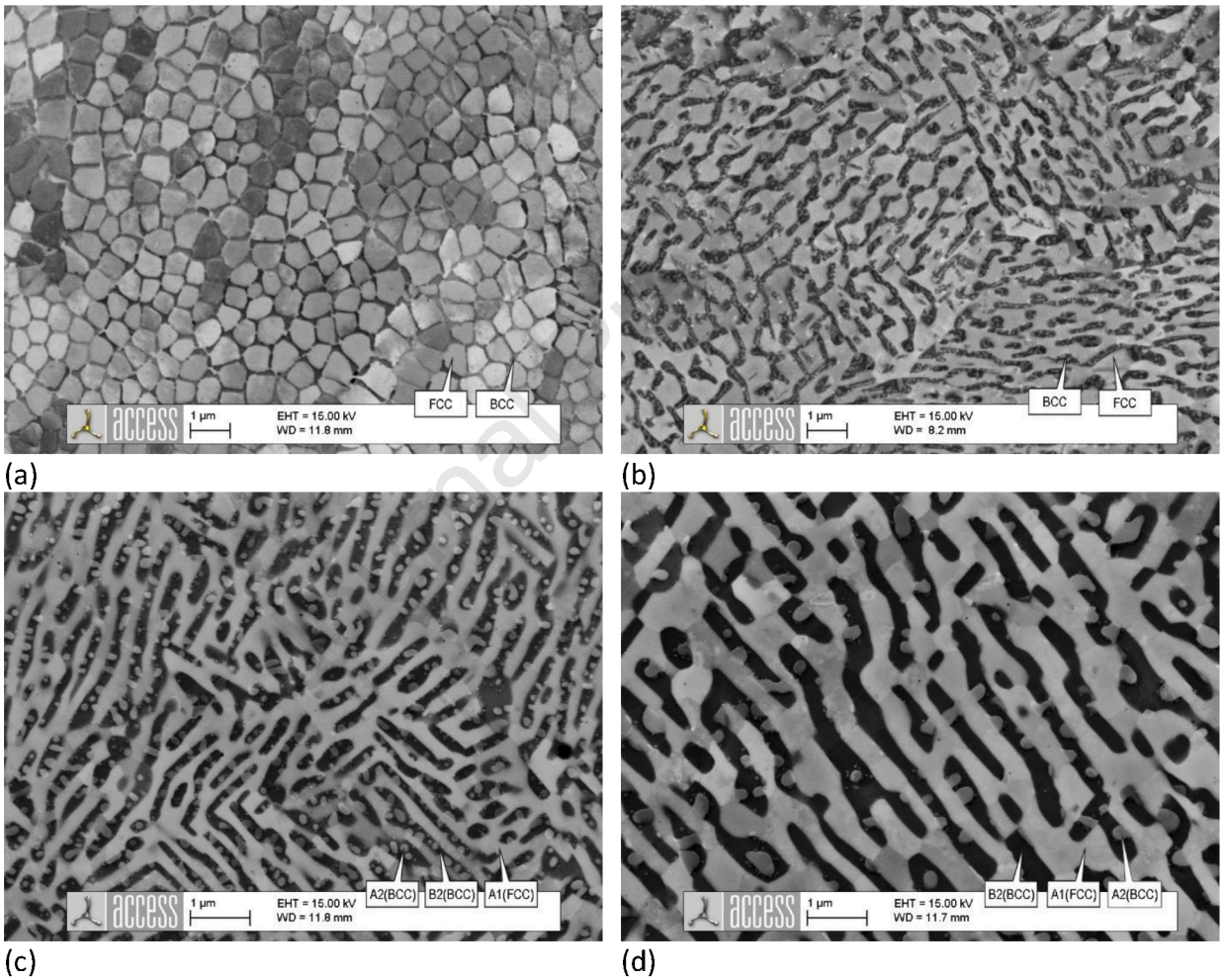

Figure 2: SEM-BSE images of the microstructure in alloy $Al_{0.75}CrFeNi_{2.1}$ in section planes perpendicular to the build direction for (a) the as-built condition and after subsequent annealing at (b) 750°C/6h, (c) 850°C/6h, (d) 950°C/6h. Note the ultrafine microstructure scale, with average spacing values ranging from 400 to 700 nm. Also note the abundant low angle grain boundaries formed in the A1(FCC) lamellae in (d). The SEM-BSE images provide Z-contrast as well as orientation contrast, the phases being A1(FCC)–bright, A2(BCC) –grey and (B2)BCC–dark grey. For convenience pointers are added to indicate the phases in the images.

Table 3: Microstructure key figures from image analysis.

Condition	Phase fractions, area%			Characteristic spacing, µm
	A1(FCC)	B2(BCC)	A2(BCC)	
LPBF as-built	85.6	14.4 (B2+A2)		Cellular spacing 0.52 ±0.13
Annealed 850°C/6h	59.9	29.3	10.8	Lamellar spacing 0.43 ±0.04
Annealed 950°C/6h	61.0	30.4	8.6	Lamellar spacing 0.67 ±0.05

The data presented in *Table 3* show that the metastable and ultrafine cellular array achieved by LPBF in the hypoeutectic alloy $Al_{0.75}CrFeNi_{2.1}$ provides means for microstructure tailoring by subsequent annealing. The phase fraction balance expressed as the FCC|BCC ratio reaches about 60|40, from an initial value of 85|15, while the microstructure retains ultrafine characteristic spacings below 1 µm.

In what follows we describe the mechanical properties of the LPBF and annealed samples based on micro-indentation and 3-point bending experiments. *Table 4* summarizes the Vickers micro-hardness and the flexural properties in comparison with as-cast samples. The mean values from several measurements are listed along with the standard deviation. The 3-point bending specimens (30x5x1.6 mm) were loaded in build direction. For each condition a representative engineering stress-strain curve is displayed in *Figure 3*.

Table 4: Mechanical properties obtained from three-point bending and micro-indentation.

Test specimen condition	Micro-indentation	Flexural properties from three-point bending		
	Microhardness, (HV0.2)	$YS_{0.2\%}$, (MPa)	UTS , (MPa)	Elongation (%)
LPBF as-built	402 ± 8	1655 ± 160	2115 ± 40	17.8 ± 0.9
LPBF+ 850°C, 6h	437 ± 4	1570 ± 50	2206 ± 40	7.2 ± 0.7
LPBF+ 950°C, 6h	387 ± 5	1303 ± 21	2098 ± 13	11.3 ± 0.7
As-cast reference	310 ± 6	762± 15	1736 ± 23	13.6 ± 1.2

The measurements reveal an outstanding strength of the as-built specimens with the flexural yield strength $YS_{0.2\%}$=1655 ± 160 exceeding by far the reference values of 762± 15 obtained in the as-cast samples. The extraordinary strength is most likely related to the contribution of dislocations to the flow stress. Indeed, high dislocation densities have been reported in FCC materials after LPBF processing, e.g. by [23] in an $Al_{0.3}CoCrFeNi$ alloy and by [24] in 316L steel,

reaching values from 10^{14} to 10^{15} m/m^3. Hence, dislocation hardening (strain hardening) during mechanical loading is limited and the difference between YS and UTS is small. At contrary, the as-cast reference materials displays remarkable strain hardening with a large difference between YS and UTS.

The annealed LPBF specimens with the highest fraction of BCC phases (around 44%) and an ultrafine microstructure display high strength at about 12% elongation. After annealing at 950°C / 6h the elongation at fracture nearly meets the value of the as-cast specimens, while retaining a 1.7 times higher yield strength. Annealing at 850°C/6h is likely not sufficient to relax the residual strains, while recovering the phase fraction balance. The elongation at facture remains poor.

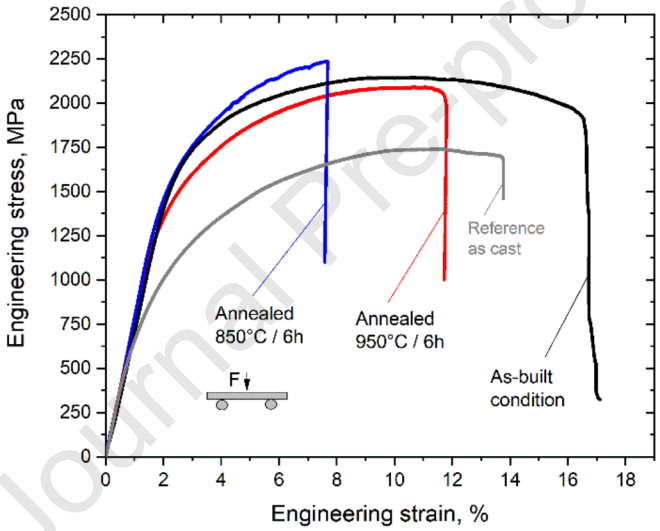

Figure 3: Representative engineering stress-strain curves from 3-point bending tests of LBFB and annealed specimens from alloy $Al_{0.75}CrFeNi_{2.1}$ compared to a reference specimen in the as-cast condition. The load (F) was applied in build direction, meaning that the tensile stresses in the specimen are transverse to the build direction.

These preliminary results provide a quick glance into the material's behavior and allow estimating where LPBF manufacturing of this alloy would rank in comparison with conventional technologies and in comparison with the Co-rich eutectic alloy $AlCoCrFeNi_{2.1}$ (see *Section 5*). A detailed analysis of mechanical properties in relation to microstructural features is beyond the scope of this article and will be presented in a follow-up article, also including data from deformation tests at elevated temperature performed under compression and with in-situ HEXRD monitoring of lattice strain evolution.

3.2. In situ observation of microstructure evolution during continuous heating

In situ observation of the microstructure evolution during heating of the LPBF as-built condition aimed at recording the phase fraction evolution as function of temperature using in situ high-energy X-ray diffraction HEXRD. The obtained data are instructive when selecting the annealing conditions for a post-build heat treatment. The material at case presents some challenges though, which relate to the difficulty of distinguishing between the ordered (B2) and disordered (A2) BCC phase on a quantitative base.

Figure 4a shows the evolution of {hkl} reflections of the A1(FCC), A2(BCC), B2(BCC) and $L1_2$ phases during heating with 20 °C/min. Initially, the LPBF as-built condition at RT presents reflections from A1, A2 and B2.

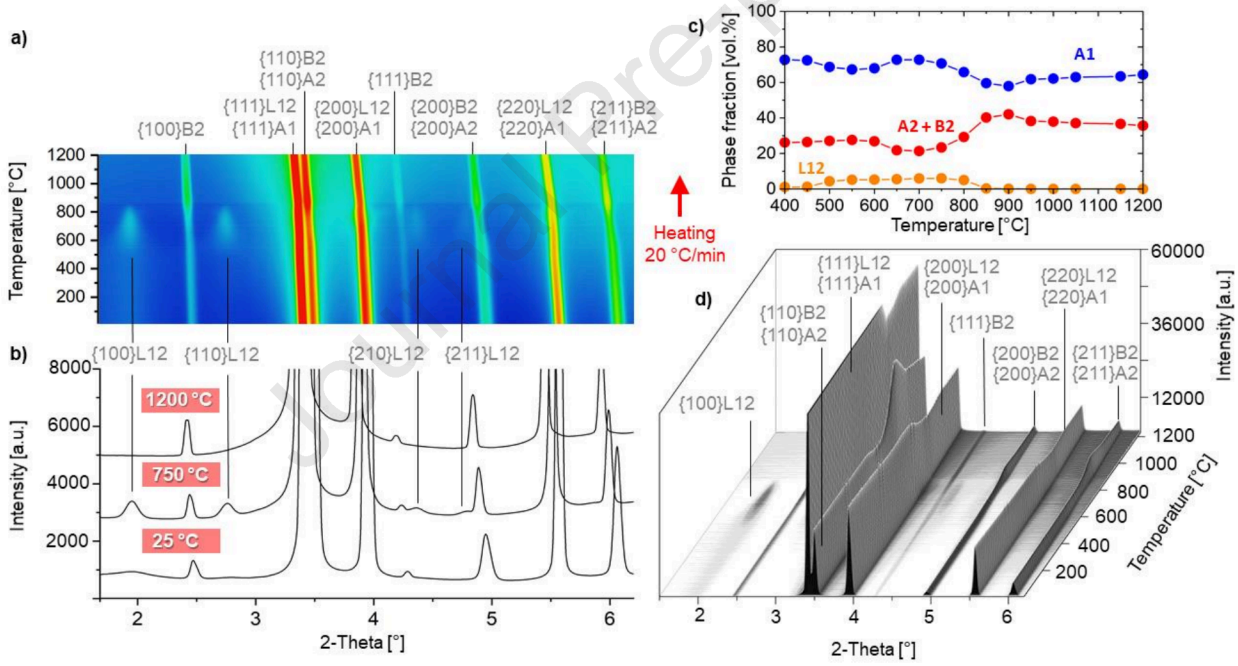

Figure 4: Evolution of {hkl} diffraction peaks of the A1, A2, B2 and $L1_2$ phases during continuous heating of the as-built alloy $Al_{0.75}CrFeNi_{2.1}$ with a heating rate of 20 °C/min (2-Theta range= 1.5-6.2º): (a) color-coded 2D plot, (b) representative portions of diffraction patterns showing the low intensity peaks and (d) entire diffractograms as a function of temperature. Quantitative results on the volume fractions of phases during heating are displayed in (c).

During heating up to ~500°C, additional reflections from {100}, {110}, {210}, {211} orientations of $L1_2$ start to appear. They remain visible up to ~800°C with phase fraction values of ~6 vol. %. $L1_2$ formation is associated with the peaks of low intensity indicated in *Figure 4b* (see diffractogram at 750°C). During the last stage of the heating (800-1200 °C), the $L1_2$ reflections are absent, while those belonging to the A1, A2, B2 phases remain visible. It is important to note that the overlapped {110}B2-{110}A2, {200}B2-{200}A2 and {200}B2-{200}A2 reflections shown in *Figure 4a* and *4d* hinder a quantitative analysis of the individual fractions of these phases. Therefore, the contribution of A2+B2 is considered together with A1 and $L1_2$ for assessing the evolution of the phase volume fractions obtained by Rietveld analysis. The results of this analysis are presented in *Figure 4c* as a function of temperature. Initially (400 °C), the fractions of A1 and A2+B2 are ~30 and ~70 vol.%, respectively. No variations are observed at lower temperatures, mainly due to the limited diffusion of chemical elements in the given time. Between 500-800 °C the formation of $L1_2$ takes place reaching up to 6 vol.%. Above ~800°C the A2+B2 fraction is seen to increase at the expense of A1 reaching a maximum of ~40 vol.% at 900°C. As the temperature increases further the amounts of A1 (60 vol.%) and A2+B2 (40 vol.%) evolve little, A1 increases and A2+B2 decreases slightly.

The results from in situ HEXRD agree fairly well with phase fraction data obtained by image analysis of 2D micrographs (compare *Table 3*). The initial FCC|BCC ratio, e.g. A1|(A2+B2) ratio, computed from HEXRD data is 70|30 (volume %) while it is 85|15 (area %) from 2D micrographs. For T=950°C HEXRD data show 60|40 (volume %), while image analysis of 2D micrographs gives 61|39 (area %).

Further on, phase equilibria were computed using Thermo-Calc and the TCHEA2 database, as displayed in *Figure 5*. They qualitatively agree with the HEXRD results regarding the presence of the $L1_2$ phase, the limit of stability of this phase being 750°C (see Figure 5a) or 800°C (see *Figure 4c*), respectively. The agreement is fairly good, keeping in mind that HEXRD measurements provide the dynamic evolution during heating with 20 K/min. Also the FCC|BCC ratios agree rather well in showing that annealing in the temperature interval from 850 to 950°C provides high fractions of BCC phases around 40%. The stability limit of the A2(BCC) could not be verified since HEXRD did not allow distinguishing between A2(BCC) and B2(BCC).

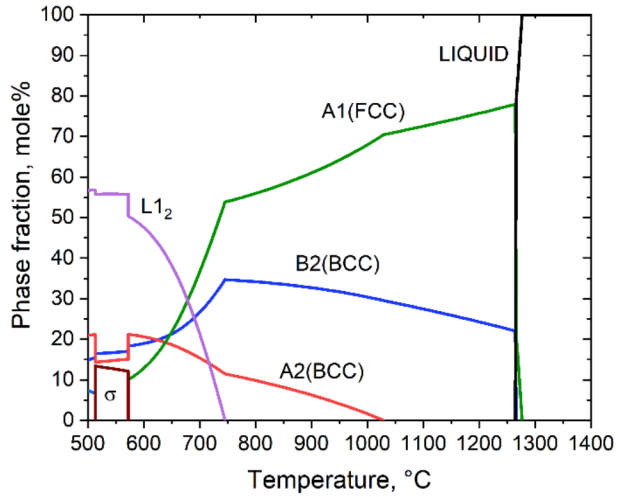

(a)

Phase equilibrium at 950°C			
Calculated	A1(FCC)	B2(BCC)	A2(BCC)
Fraction	64.2	31.7	4.1
Al, at.%	8.4	32.7	0.8
Cr, at.%	24.1	5.0	77.2
Fe, at.%	25.1	10.9	17.8
Ni, at.%	42.4	51.4	4.2

Thermo-Calc software, Database TCHEA2

(b)

Figure 5: Phase equilibria for alloy Al15.4-Cr19.6-Fe20.9-Ni44.1 (at. %), i.e. $Al_{0.75}CrFeNi_{2.1}$ computed with the Thermo-Calc software and the database TCHEA2 showing (a) the phase fractions as function of temperature and (b) phase fractions and compositions for T=950°C.

The computed phase composition data for equilibrium at T=950°C (*Figure 5b*) are further used in section 3.3, where they serve for comparison with APT measurements.

3.3 Microstructure characterization by atom probe tomography

Due to high solidification rates associated with the LPBF manufacturing process the microstructure results in ultrafine and nano-scale features. Therefore, the information from SEM-based characterization methods is not sufficiently accurate to provide reliable data about the chemistry of the FCC and BCC phases and their interphase boundaries. To address these issues, further investigations were performed using 3-dimensional atom probe tomography (APT), which provides a high level of elemental detection sensitivity while also allowing for a site-specific specimen preparation [25]. The technique has been successfully applied to high entropy alloys [26] providing valuable insight into chemical heterogeneities, precipitation, and interface segregation.

3.3.1 Atom probe tomography (APT) of a sample in the as-built condition

A tip-shaped specimen was extracted for APT by FIB cutting from an LPBF sample in the as-built condition, such that it extends from the cellular FCC phase at the specimen base to the

intracellular BCC phase at its tip, thereby encompassing the FCC/BCC interphase boundary. Figures 6a and 6b display the corresponding APT atom maps. Three distinct phases were observed; namely A1(FCC), B2(BCC) and A2(BCC). The A1(FCC) phase is a solid solution phase, the B2(BCC) is a Ni- and Al-rich ordered phase, while A2(BCC) is a Cr- and Fe-rich disordered phase. The B2 and A2 phases appear as products of a spinodal decomposition reaction related to the miscibility gap of the primary B2 phase and are denoted B2# and A2#. At the FCC/BCC phase boundary a thin film of the B2(BCC) phase can be distinguished, being termed B2 because its composition is slightly different from that of B2#. The phase composition in the distinct regions were analyzed by APT and the results are summarized in *Table 5* also including impurities such as as Mn and Si. It is clear from *Table 5* that the primary A1(FCC) phase composition is close to the integral alloy composition (see *Table 1*), while recalling that it grew under strongly out-of-equilibrium conditions. Proximity histograms (proxigrams for short) were plotted across the A1(FCC) and B2(BCC) interphase (*Figure 6c*) and across the interphase in the spinodally decomposed region (*Figure 6d*), respectively. From these two proxigrams, it is clear that there is no segregation of elements at the interphase boundaries.

Table 5: Phase composition of different phases analyzed by APT in the as-built LPBF sample.

Crystal structure	Element content (at.%)					
	Al	**Cr**	**Fe**	**Ni**	**Mn**	**Si**
A1(FCC)	14.95	21.36	21.83	41.75	0.07	0.04
B2(BCC)	30.64	5.76	10.62	52.88	0.06	0.04
B2(BCC)# spinodal	28.30	9.12	12.10	50.38	0.06	0.04
A2(BCC)# spinodal	4.50	52.52	30.30	12.58	0.06	0.04

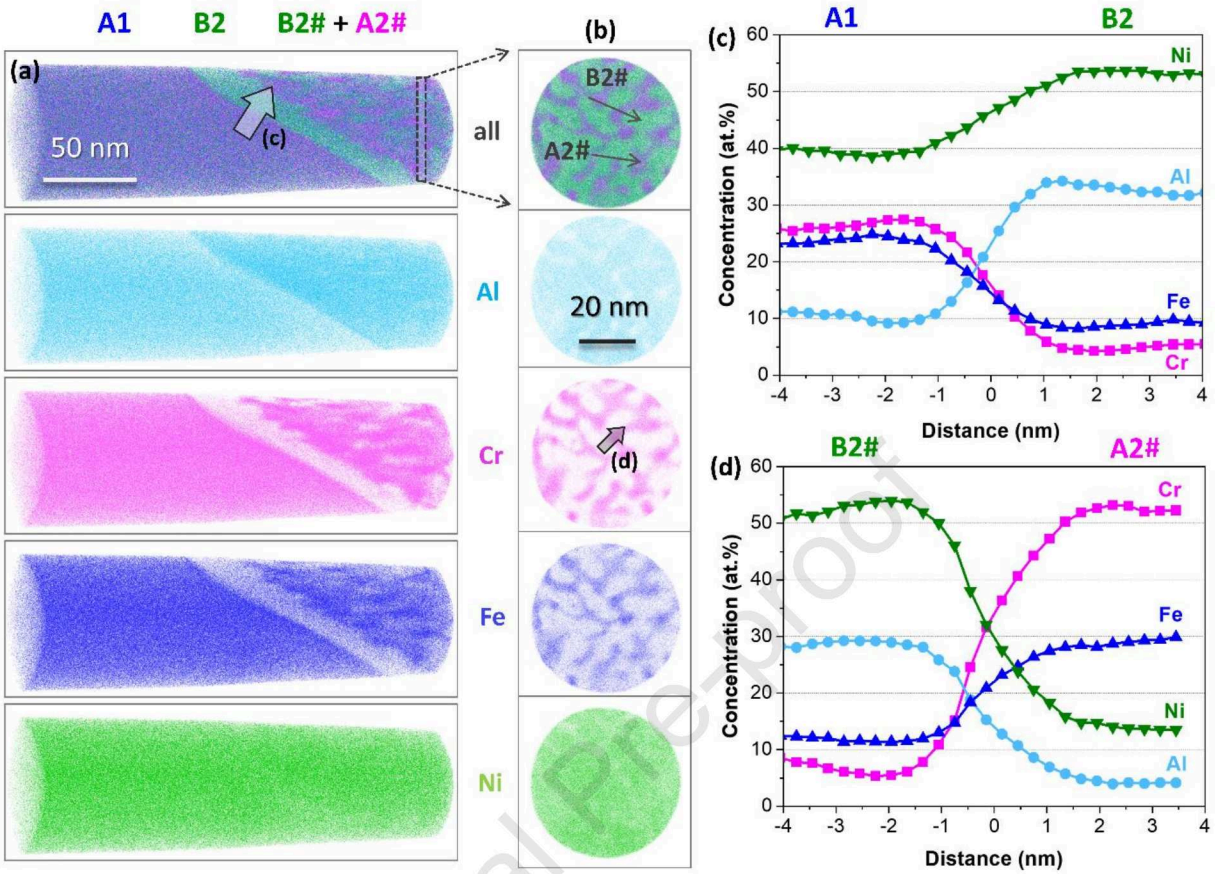

Figure 6: APT analysis of the alloy $Al_{0.75}CrFeNi_{2.1}$ in the as-built condition (a) APT atom maps of Ni, Al, Fe and Cr comprising different phases, (b) a thin slice view of the spinodally decomposed BCC region, (c) proximity histogram across the A1|B2 phase boundary and (d) proximity histogram across the B2#|A2# phase boundary.

3.3.2 Atom probe tomography (APT) of a sample after isothermal annealing at 950°C, 6 h

A tip-shaped specimen was extracted for APT by FIB cutting from an LPBF sample in the annealed condition (950°C/6h), such that it extends over three phases, i.e. A1(FCC) at the specimen base, B2(BCC) and finally A2(BCC) at the specimen tip, thereby encompassing two interphase boundaries. *Figure 7* shows the corresponding APT atom maps. The bulk composition of the identified phases was analyzed by APT and the results are summarized in *Table 6*. Compared to the as-built condition (see *Table 5*), it is clearly evident that the heat treatment modifies the composition of the phases following the microstructure evolution towards phase equilibrium. The A1(FCC) phase shows a marked decrease in Al and an increase in Fe, while Cr and Ni are moderately changing. The B2(BCC) phase attains a sharper stoichiometry close to the NiAl

compound. The A2(BCC) phase, initially rich in Fe turns to be Cr-rich. In fact the chemical composition of the phases measured by APT is in very good agreement with Thermo-Calc predictions (compare *Figure 5b*).

Table 6: Phase composition of different phases analyzed by APT in the sample annealed at 950°C/6h.

Crystal structure	Element content, at.%					
	Al	**Cr**	**Fe**	**Ni**	**Mn**	**Si**
A1(FCC)	5.065	23.83	31.50	39.52	0.02	0.07
B2(BCC)	34.80	1.28	8.30	55.57	0.04	0.01
A2(BCC)	0.21	82.75	14.43	2.53	0.04	0.03

The atom maps in *Figure 7a* contain two interphase boundaries, i.e. A1(FCC)|B2(BCC) and B2(BCC)|A2(BCC), respectively. The chemical composition profiles across these interphase boundaries are displayed in *Figure 7b* and *7c* as proximity histograms. No segregation was evidenced at the A1(FCC)|B2(BCC) boundary (*Figure 7b*), however Fe is slightly enriched at the B2(BCC)|A2(BCC) boundary (*Figure 7c*).

Interestingly, Ni-rich precipitates (or nanoclusters) were observed inside the A2(BCC) phase. A detailed APT investigation was performed and is shown in *Figure 8a*. The precipitates are likely formed during water quenching after the annealing treatment. Their size is in the range of 5-10 nm and their composition is close to a $Al_{0.25}CrFeNi_{2.5}$ stoichiometry. Interestingly, the Al-content in these precipitates is quite low. Perhaps, it is the early stage precipitation of B2(BCC), but this is a hypothesis for now. A proximity histogram across the interphase is presented in *Figure 8b*.

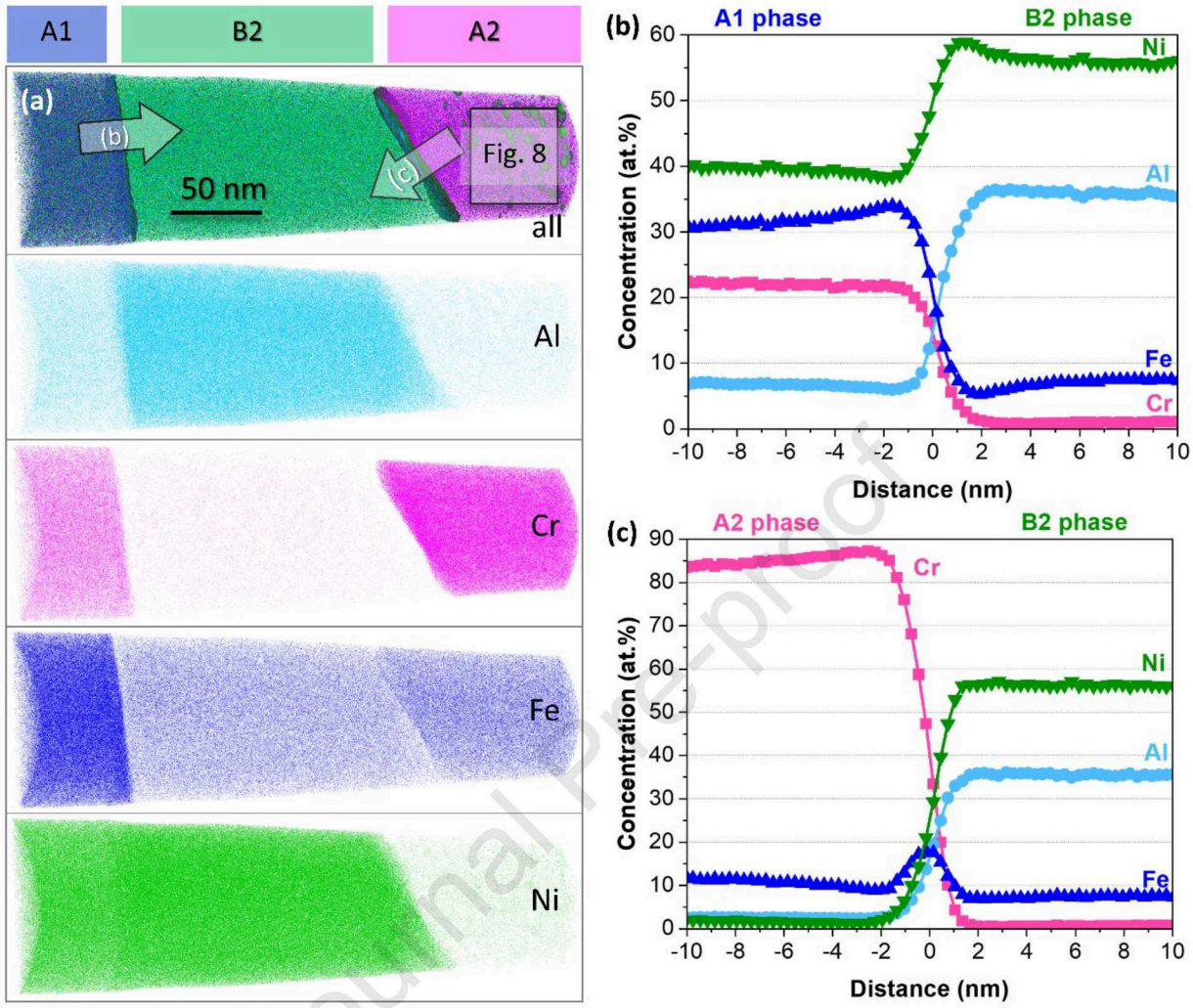

Figure 7: APT analysis of the alloy $Al_{0.75}CrFeNi_{2.1}$ after annealing at 950°C for 6 h followed by water quenching (a) APT atom maps of Al, Cr, Fe and Ni, (b) proximity histogram across the A1(FCC)|B2(BCC) phase boundary and (c) proximity histogram across the A2(BCC)|B2 (BCC) phase boundary.

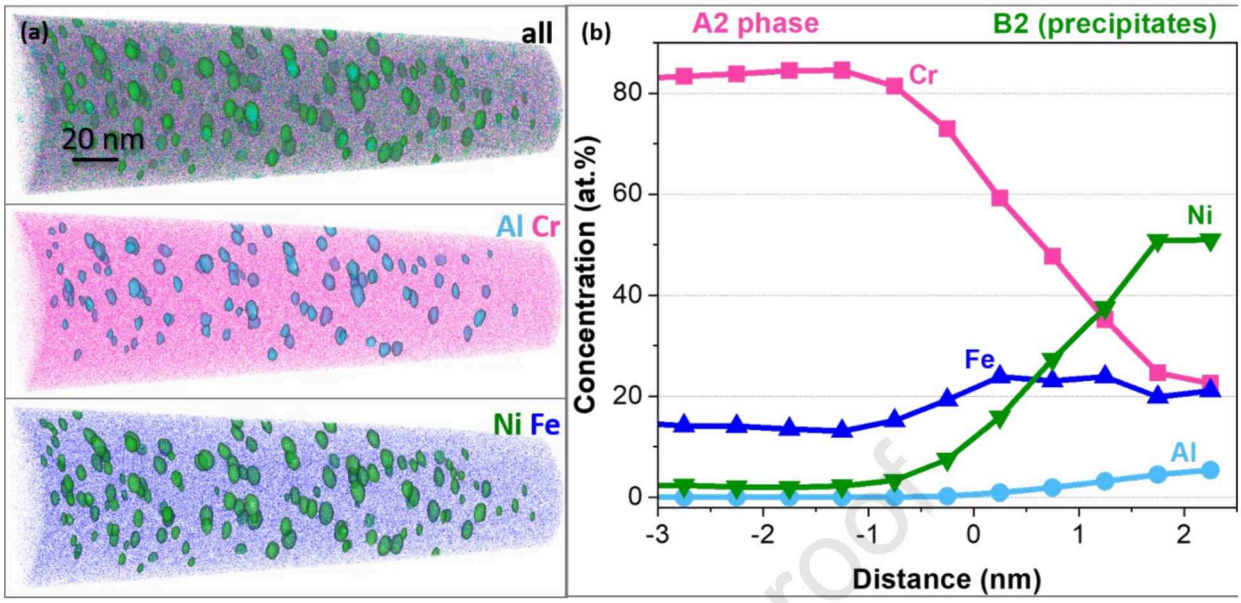

Figure 8: Detailed APT analysis of the A2(BCC) phase formed in alloy $Al_{0.75}CrFeNi_{2.1}$ after annealing at 950°C for 6 h followed by water quenching: (a) APT atom maps of Al, Cr, Fe and Ni with isosurface values of 1 at% and 10 at% for Al and Ni, respectively and (b) proximity histogram across the matrix | precipitate phase boundary.

Finally, *Figure 9a* shows yet another detail related to quenching: The APT atom maps clearly show precipitates at a low angle grain boundary (LAGB) of the A1(FCC) phase. The GB displays pronounced enrichment of Ni and Al which is rather a discontinuous layer of nano-size precipitates. *Figure 9b* shows the atomic density maps of the GB in-plane view (aerial view). A concentration profile across the LAGB in *Figure 9c* clearly shows the enrichment of Ni, Al and depletion of Fe, Cr. From the proxigram across the GB in *Figure 9d* we conclude that the precipitate stoichiometry is close to Ni_3Al ($L1_2$). We attribute the formation of these GB precipitates to quenching, since the HEXRD results as well as thermodynamic computations agree on the stability limit of the $L1_2$ phase being below 800°C

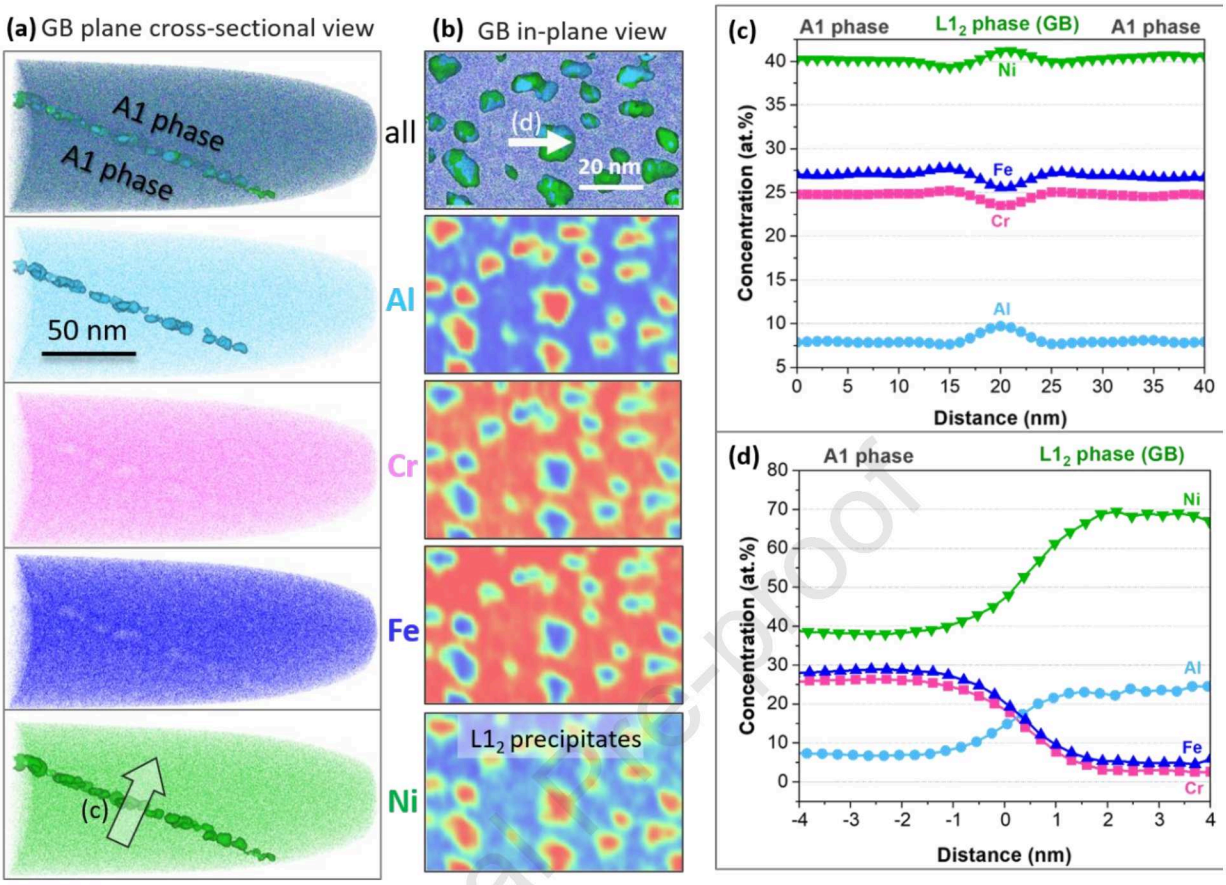

Figure 9: Detailed APT analysis of a low angle grain boundary (LAGB) inside the (A1)FCC phase in alloy $Al_{0.75}CrFeNi_{2.1}$ after annealing at 950°C for 6 h followed by water quenching. (a) APT atom maps with grain boundary cross-sectional view (side view), (b) heat maps for major alloying constituents of the same grain boundary in-plane view, (c) concentration profile across the GB and (d) proximity histogram across the A1(FCC) phase and the $L1_2$ precipitates.

4. Discussion

The research presented here entrained several experimental and computational techniques combined in the effort to understand the origin and evolution of the multi-scale microstructure in the hypo-eutectic alloy $Al_{0.75}CrFeNi_{2.1}$ produced by LPBF. Novel insights were gained from the results, as discussed below. The discussion refers to (a) the alloy design concept, (b) the solidification microstructure under LPBF conditions, (c) the evolution of a quasi-lamellar microstructure upon post-build annealing treatments and (d) the mechanical properties achieved in comparison to reference materials.

(a) The alloy design targeted a hypo-eutectic composition, aiming at an FCC-rich solidification microstructure with low propensity to crack formation during LPBF processing. The quaternary composition space offers several options for designing a hypo-eutectic alloy, i.e. an alloy with primary FCC solidification. However, aluminum is the strongest BCC-stabilizing element mainly due to its large atom size [27] and therefore a small reduction of the aluminum content was considered to be the most effective strategy. Reducing the aluminum content from 16.6 at.% (eutectic $Al_{0.8}CrFeNi_{2.1}$) to a nominal value of 15.5 at.% (hypo-eutectic $Al_{0.75}CrFeNi_{2.1}$) indeed allowed LPBF processing with a baseplate preheating of 200°C, which is feasible for most industrial 3D printing devices. For future powder batches the content and margins for Aluminum can be specified as 15.5 $\pm$0.5 at.%. With this, the risk of accidentally moving to the hyper-eutectic side with primary B2(BCC) phase formation and potential cracking can be avoided.

(b) The solidification of the alloy $Al_{0.75}CrFeNi_{2.1}$ under LPBF conditions is accomplished by cellular growth of the primary (A1)FCC phase. A thin envelope of the BCC phase(s) forms around the cells. APT measurements show that the intercellular BCC is spinodally decomposed into B2(BCC) and A2(BCC). In the as-built condition the FCC|BCC ratio is 85|15 (area %) when measured by image analysis in 2D micrographs, and 70|30 (volume %) when evaluated from HEXRD data. The cellular spacing is ultrafine with values around 0.5 µm. The thin intercellular liquid channels are nano-sized and too narrow to accommodate any coupled eutectic growth. We propose that the absence of intercellular coupled eutectic growth is due to spatial confinement in the cellular array. This argument is supported by the results from phase-field modelling of cellular growth in

a Ni-base alloy [28]. The authors [28] analyzed the fraction solid evolution in a cellular array under LPBF conditions and showed that the fraction-solid curves display a sharp increase reminiscent of a truncated Scheil-type behavior [29]. For the hypo-eutectic alloy at case a similar behavior would indeed leave no space to accommodate any intercellular coupled eutectic growth. At contrary, the EHEA alloy $AlCoCrFeNi_{2.1}$ with eutectic composition processed by LPBF [16] was reported to show coupled eutectic growth leading to a nano-lamellar solidification pattern.

(c) Post-build annealing treatments were applied to the alloy $Al_{0.75}CrFeNi_{2.1}$ aiming at stress relaxation and microstructure evolution towards thermodynamic equilibrium. During annealing the as-built microstructure transforms from a cellular to a quasi-lamellar pattern and the FCC|BCC phase ratio approaches ~60|40 %. This is a novel pathway to quasi-lamellar microstructures achieved by solid state growth of BCC phases and coarsening. The lamellar appearance and the associated alinement of FCC| BCC phase boundaries is attributed to a pronounced anisotropy of the FCC|B2(BCC) phase boundary energy. Even if quantitative data about the phase boundary energy landscape are lacking, we think that anisotropy is the key to understand this transformation in detail. Recently, embedded atom model (EAM) interatomic potentials were published for Fe–Ni–Cr–Co–Al high-entropy alloys [30] and may be used to compute the phase boundary energy landscape using e.g. molecular dynamics computations.

Optimum annealing temperatures were identified to range from 850 to 950°C. Following HEXRD results this temperature interval is convenient, since it allows for a fast equilibration of the FCC|BCC phase fraction balance to ~60|40 volume %. For annealing durations up to 6 hours the lamellar spacing remains ultrafine, ranging around 0.5 to 0.6 µm. HEXRD also revealed the existence of the $L1_2$ phase and its dissolution above T≈800°C in rather good agreement with thermodynamic computations. APT measurements revealed nano-sized $L1_2$ precipitates decorating a low angle grain boundary (LAGB) of the FCC phase in a specimen annealed at 950°C for a duration of 6 hours followed by water quenching. These $L1_2$ precipitates likely formed during quenching. Another quenching effect was revealed for the A2(BCC) phase, which contains nano-scale precipitates of B2(BCC).

Finally, and worth pointing out, are the options to carry out annealing treatments at higher temperature and for shorter durations, e.g. at 1050°C for 1 hour. These options were not explored here, but offer the chance to equilibrate the microstructure in the two-phase field A1(FCC)+B2(BCC), i.e. above the stability limit of the A2(BCC) phase (compare *Figure 5a*). The A2(BCC) phase would from upon cooling with a significantly finer size, being excluded from coarsening.

(d) The mechanical properties of the hypoeutectic alloy $Al_{0.75}CrFeNi_{2.1}$ were evaluated by micro-indentation and three-point bending for the LPBF as-built and annealed conditions. The measurements revealed an outstanding strength of the as-built specimens with the flexural yield strength reaching 1655 $\pm$ 160 MPa. The tensile yield strength was estimated to be 1092$\pm$ 106 MPa by applying a conversion factor of 0.66. These values exceed by far the reference values obtained in as-cast samples being 762 $\pm$ 15 MPa (flexural) and 503 MPa (tensile), respectively. Noteworthy is the good strength / ductility balance obtained in the as-built condition with elongations at fracture about 18% for an ultimate tensile strength of about 1395 MPa. Future applications of the material in the as-built condition may however be limited, since martensitic stainless steels, i.e. the age hardenable steels 17-4PH, 15-5PH [31, 32] or the newly developed low cost steel AF9628 are competitive [33]. By means of illustration we quote tensile properties of the 17-4PH steel from Zai et al. [31] with YS values ranging from 945 to 1005 MPa, UTS values from 1319 to 1417 MPa, and elongations at fracture from 11 to 15.5 %. These values refer to LPBF specimens in distinct heat treated conditions. Potential applications are rather expected for elevated temperatures up to 650 or 700°C, where the presence of the lamellar B2(BCC) phase in the microstructure is deemed beneficial. The prolonged annealing treatment at 950°C for a duration of 6 hours was investigated along this line of arguments. Compared to the as-built condition the flexural yield strength after 950°C annealing is reduced to 1303 $\pm$ 21 MPa (compare *Table 4* and *Figure 3*). The corresponding tensile yield strength is estimated to be 860 $\pm$ 21 MPa, the ultimate strength reaches 1384 $\pm$ 9 MPa with an elongation at fracture of 11.3 $\pm$ 0.7 %. These properties compare well with the ones reported in [34] for the EHEA alloy $AlCoCrFeNi_{2.1}$ after severe hot rolling with 70% thickness reduction followed by a two-step annealing treatment [11].

Superior room temperature properties pertain to heavily cold-rolled $AlCoCrFeNi_{2.1}$ after short recrystallization annealing [10, 11].

Figure 10 presents the mechanical properties achieved in the present work in comparison with the EHEA alloy $AlCoCrFeNi_{2.1}$ manufactured along distinct processing routes, i.e. casting, hot rolling, cold rolling and LPBF.

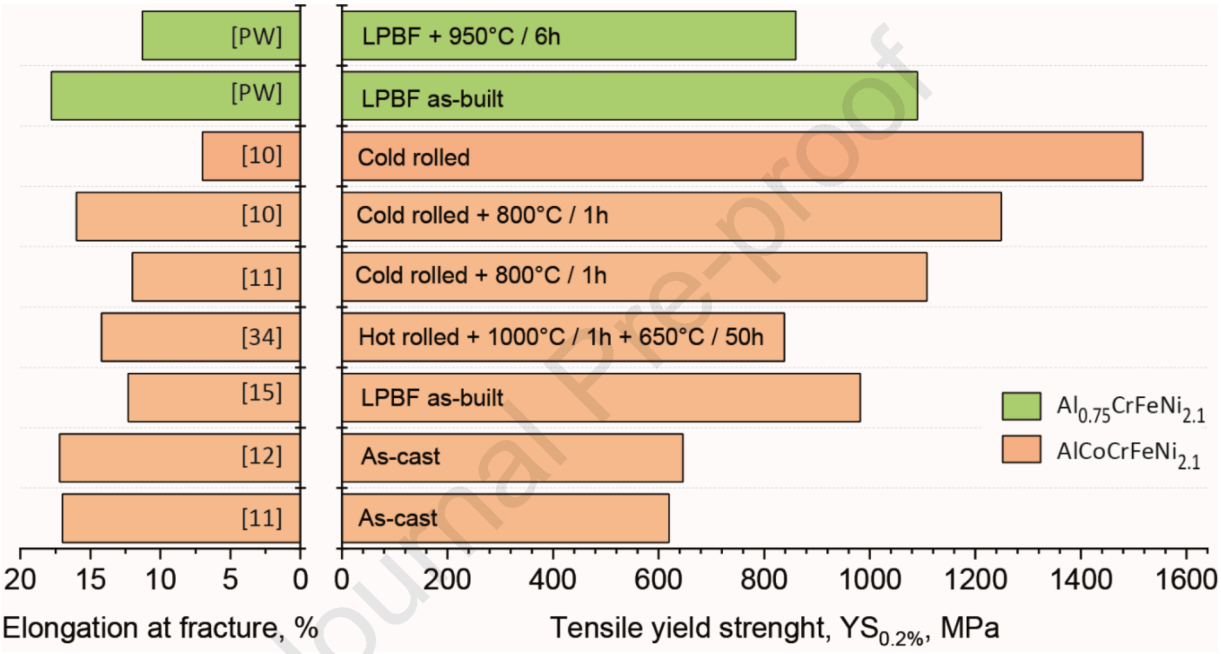

Figure 10: Overview of mechanical properties reported for the EHEA alloy $AlCoCrFeNi_{2.1}$ manufactured along distinct processing routes [10,11,12,15, 34] along with the data obtained in the present work [PW] for the Co-free hypo-eutectic alloy $Al_{0.75}CrFeNi_{2.1}$. For comparison the tensile yield strength was estimated from the flexural yield strength using a conversion factor of 0.66 [PW].

The cold rolling data correspond to 90% thickness reduction in multiple passes [10] and are meant to highlight the dislocation hardening as a prominent mechanism. Annealing at 800°C for 1h suffices to achieve nearly complete [10] or fully complete recrystallization of the phases [12]. The recrystallized grain size remains small around 0.45 µm, as an average over FCC and BCC grains. This ultrafine size is roughly comparable to the quasi-lamellar spacing obtained after annealing at 950°C /6h in the present work. Phase fractions finally, are also comparable, being 65% FCC /

35% BCC in $AlCoCrFeNi_{2.1}$ [10] and 56% FCC / 44% BCC in the annealed $Al_{0.75}CrFeNi_{2.1}$ alloy. The hot rolling data [34] correspond to 70% thickness reduction at 800°C and a two-step subsequent annealing treatment at 100°C/1h plus 600°C/50h.

From the comparison we conclude that LPBF processing with a prolonged post-build annealing heat treatment at T≈950°C is a competitive and promising process route for the Co-free hypoeutectic alloy $Al_{0.75}CrFeNi_{2.1}$ alloy. Superior properties were recently reported for $AlCoCrFeNi_{2.1}$ with a nano-lamellar microstructure obtained by LPBF processing followed by short duration annealing at 800°C and 1000°C for 1 hour, respectively [16].

One questions remains open: why is the strength of the annealed LPBF specimens about 1.7 times higher compared to as-cast reference specimens and also compared to reported values for the as-cast EHEA alloy $AlCoCrFeNi_{2.1}$ [11, 12, 16]?. The major strengthening contributions come from size hardening associated to the ultrafine microstructure, but a significant contribution must likely be attributed to the subgrain structure of the phases, readily visible in the FCC phase (compare *Figure 2d* and *Figure 9*). Low angle grain boundaries (LAGB) are abundantly formed during annealing, being a sign of stress relaxation and recovery of strain. A quantitative analysis of the LAGB fraction and disorientation distribution has not been performed in this study, but is required for a more comprehensive analysis of the material properties obtained along the LPBF route. A good overview of substructure strengthening mechanisms associated with dislocation cells and LAGBs is found in [35], while [36] contains a recent application to the case of austenitic materials processed by LPBF.

5. Conclusions

Based on the research results we conclude that the LPBF manufacturing of the Co-free, hypo-eutectic alloy $Al_{0.75}CrFeNi_{2.1}$ is technologically feasible and provides a material with a novel microstructure and very promising properties. The major findings are outlined as follows:

(1) Under LPBF conditions the alloy solidifies with an FCC-rich cellular pattern and a cell spacing of about 0.5 µm. The densely packed cellular array prevents coupled eutectic growth in the

intercellular liquid. Instead, a thin BCC layer develops, being spinodally decomposed into A2(BCC) and B2(BCC) phases.

(2) Upon annealing the cellular pattern transforms to a quasi-lamellar pattern by solid state growth of BCC phases and coarsening. We captured early stages of this transformation (compare *Figure 2b*) and conjecture that the anisotropy of the FCC|B2(BCC) phase boundary energy plays a key role in this transformation, being the reason for the phase boundary alignment in the evolving lamellar pattern.

(3) After annealing for 6 hours at 950°C the novel microstructure displays a lamellar spacing of about 0.67 µm. The FCC|BCC phase ratio reaches 60|40 % with the fraction of B2(BCC) being about 30%. The B2(BCC) phase with a composition nearly matching the intermetallic NiAl compound is expected to confer the necessary strength, when envisaging applications at elevated temperatures.

(4) In the as-built condition the tensile properties, estimated from three-point bending measurements, are YS ≈1092 MPa, UTS ≈1395 MPa and a total elongation of 17,8 %, being comparable to martensitic steels and exceeding by far the as-cast reference material. After annealing (950°C, 6h) the achieved properties, YS ≈860 MPa, UTS ≈1378 MPa and total elongation of 11,3 %, are comparable to the EHEA alloy $AlCoCrFeNi_{2.1}$ after hot-rolling and annealing.

A detailed analysis of the mechanical properties in relation to microstructural features was beyond the scope of this article and will be presented in a dedicated paper, also including data from deformation tests at elevated temperature performed under compression and with in-situ HEXRD monitoring of lattice strain evolution.

Acknowledgements

The Deutsches Elektronen-Synchrotron (DESY) is acknowledged for the provision of synchrotron radiation facilities in the framework of proposal I-20210694. P. Barriobero-Vila acknowledges financial support from the Spanish Ministry of Science through the Ramón y Cajal grant RYC2020-029585-I. N. Navaeilavasani, S. Gein, I. Cazic and U. Hecht acknowledge funding through the

INNO-KOM program under grant 49VF180027 by the German Ministry of Economics and Energy (BMWi). Special thanks are due to M. Knieps from Oerlikon AM Europe GmbH for powder characterization. A. Vayyala acknowledges RWTH Aachen University within the framework of the Collaborative Research Centre (SFB 1120) "Precision Melt Engineering" funded by the German Research Foundation (DFG e.V.).

Data availability

The authors confirm that the data supporting the findings of this study are available within the article. The digital data and metadata that support the findings of this study are available from the corresponding author [UH] upon reasonable request.

References

[1] A. Regordosa, J. Sertucha, J.R. Olaizola, J. Lacaze, When is a Cast Iron Eutectic?, Inter Metalcast 16, (2022) 119–131. https://doi.org/10.1007/s40962-021-00587-7.

[2] H. Ye, An overview of the development of Al-Si-Alloy based material for engine applications, J. of Mater. Eng. and Perform. 12 (2003) 288–297. https://doi.org/10.1361/105994903770343132.

[3] C.S.Tiwary, P. Pandey, S. Sarkar, R. Das, S. Samal, K. Biswas, K. Chattopadhyay, Five decades of research on the development of eutectic as engineering materials, Prog. Mater. Sci. 123 (2022) 100793. https://doi.org/10.1016/j.pmatsci.2021.100793.

[4] D. Röhrens, N. Navaeilavasani, O. Stryzhyboroda, F. Swientek, P. Pavlov, D. Meister, A. Genau, U. Hecht, Microstructure and Mechanical Properties of BCC-FCC Eutectics in Ternary, Quaternary and Quinary Alloys From the Al-Co-Cr-Fe-Ni System, Front. Mater. 7 (2020) 567793. https://doi.org/10.3389/fmats.2020.567793.

[5] A. Misra, R. Gibala, Room-temperature deformation behavior of directionally solidified multiphase Ni-Fe-Al alloys, *Met Mat Trans. A*28 (1997) 795–807. https://doi.org/10.1007/s11661-997-0066-x.

[6] X. Jin, J. Bi, L. Zhang, Y. Zhou, X. Du, Y. Liang, B. Li , A new CrFeNi2Al eutectic high entropy alloy system with excellent mechanical properties, J. Alloys Compd. 770 (2019) 655–661. https://doi.org/10.1016/j.jallcom.2018.08.176.

[7] Y. Lu, Y. Dong, S. Guo, L.Jiang, H. Kang, T. Wang, B. Wen, Z. Wang, J. Jie, Z. Cao, H. Ruan, T. Li, A Promising New Class of High-Temperature Alloys: Eutectic High-Entropy Alloys, Sci. Rep. 4 (2014) 6200. https://doi.org/10.1038/srep06200.

[8] X. Gao, Y .Lu, B. Zhang, N. Liang, G. Wu, G. Sha, J. Liu, Y. Zhao, Microstructural origins of high strength and high ductility in an AlCoCrFeNi2.1 eutectic high-entropy alloy, Acta Mat. 141 (2017) 59–66, https://doi.org/10.1016/j.actamat.2017.07.041.

[9] L. Wang., C.Yao, J. Shen, Y. Zhang, T.Wang, Y. Ge, L. Gao, G. Zhang, Microstructures and room temperature tensile properties of as-cast and directionally solidified AlCoCrFeNi2.1 eutectic high-entropy alloy, Intermetallics 118 (2020) 106681, https://doi.org/10.1016/j.intermet.2019.106681.

[10] A. Lozinko, R. Gholizadeh, Y .Zhang, U. Klement, N. Tsuji, O.V. Mishin, S. Guo, Evolution of microstructure and mechanical properties during annealing of heavily rolled AlCoCrFeNi2.1 eutectic high-entropy alloy, Mat. Sci. Eng A 833 (2022) 142558. https://doi.org/10.1016/j.msea.2021.142558.

[11] I.S. Wani, T. Bhattacharjee, S. Sheikh, P.P. Bhattacharjee, S. Guo, N. Tsuji, Tailoring nanostructures and mechanical properties of AlCoCrFeNi2.1 eutectic high entropy alloy using thermo-mechanical processing, Mat. Sci. Eng A 675 (2016) 99–109. https://doi.org/10.1016/j.msea.2016.08.048.

[12] T. Xiong, S. Zheng, J. Pang, X. Ma, High-strength and high-ductility AlCoCrFeNi2.1 eutectic high-entropy alloy achieved via precipitation strengthening in a heterogeneous structure, Scripta Mat. 186 (2020) 336–340. https://doi.org/10.1016/j.scriptamat.2020.04.035.

[13] C. Feng, X. Chai, Z. Sun, X Liu, J. Wang, X. Tao, F. Chen, G. Xu, Y. Cui, Hierarchical eutectic structure and superior mechanical property in low cobalt content $AlCo_{0.2}CrFeNi_{2.1}$ alloy by laser metal deposition, J. Alloys Compd. 915 (2022) 165400. https://doi.org/10.1016/j.jallcom.2022.165400.

[14] L. Huang, Y. Sun, N. Chen, H. Luan, G. Le, X. Liu, Y. Ji, Y. Lu, P. K. Liaw, X. Yang, Y. Zhou, J. Li, Simultaneously enhanced strength-ductility of AlCoCrFeNi2.1 eutectic high-entropy alloy via additive manufacturing, Mat. Sci. Eng. A 830 (2022) 142327. https://doi.org/10.1016/j.msea.2021.142327

[15] L. He, S. Wu, A. Dong, H. Tang, D. Du, G. Zhu, B. Sun, W. Yan, Selective laser melting of dense and crack-free AlCoCrFeNi2.1 eutectic high entropy alloy: Synergizing strength and ductility, Journal of Mater. Sci. Technol. 117 (2022) 133–145. https://doi.org/10.1016/j.jmst.2021.11.049.

[16] J. Ren, Y. Zhang, D. Zhao, D. *et al.,* Strong yet ductile nanolamellar high-entropy alloys by additive manufacturing, Nature 608 (2022) 62–68. https://doi.org/10.1038/s41586-022-04914-8.

[17] N. Schell, A. King, F. Beckmann, T. Fischer, M. Müller, A. Schreyer, The High Energy Materials Science Beamline (HEMS) at PETRA III, Mater Sci Forum 772 (2013) 57–61. https://doi.org/10.4028/www.scientific.net/msf.772.57.

[18] P. Staron, T. Fischer, T. Lippmann, A. Stark, S. Daneshpour, D. Schnubel, E. Uhlmann, R. Gerstenberger, B. Camin, W. Reimers, E. Eidenberger, H. Clemens, N. Huber, A. Schreyer, In situ experiments with synchrotron high-energy X-rays and neutrons, Adv. Eng. Mater A 13 (2011) 658–663. https://doi.org/10.1002/adem.201000297.

[19] J. Schindelin, I. Arganda-Carreras, E. Frise, V. Kaynig, M. Longair, T. Pietzsch, A. Cardona, Fiji: an open-source platform for biological-image analysis, Nat. Methods 9(7) (2012) 676–682. https://doi.org/10.1038/nmeth.2019.

[20] A. Hammersley, S.O. Svensson, A. Thompson, Calibration and correction of spatial distortions in 2D detector systems. Nucl. Instrum. Methods. Phys. Res. A 346 (1994) 312–321. https://doi.org/10.1016/0168-9002(94)90720-X.

[21] L. Lutterotti, S. Matthies, H.R. Wenk, A.J. Schultz, J. Richardson, Combined texture and structure analysis of deformed limestone from time-of-flight neutron diffraction spectra, J. Appl. Phys. 81 (1997) 594–600. https://doi.org/10.1063/1.364220.

[22] G. Boussinot, M. Apel, J. Zielinski, U. Hecht, J. H. Schleifenbaum, Strongly out-of-equilibrium columnar solidification during laser powder-bed fusion in additive manufacturing, Phys. Rev. Appl. 11(1) (2019) 014025. https://doi.org/10.1103/PhysRevApplied.11.014025.

[23] F. Peyrouzet, D. Hachet, R. Soulas, C. Navone, S. Godet, S. Gorsse, Selective Laser Melting of Al0.3CoCrFeNi High-Entropy Alloy: Printability, Microstructure, and Mechanical Properties, JOM 71 (2019) 3443–3451, https://doi.org/10.1007/s11837-019-03715-1.

[24] Y.J. Yin, J. Q. Sun, J. Guo, X.F. Kan, D.C. Yang, Mechanism of high yield strength and yield ratio of 316 L stainless steel by additive manufacturing, Mat. Sci. Eng. A 744 (2019) 773–777. https://doi.org/10.1016/j.msea.2018.12.092.

[25] K. Thompson, D. Lawrence,D.J. Larson, J.D. Olson, T.F. Kelly, B. Gorman, In situ site-specific specimen preparation for atom probe tomography, Ultramicroscopy 107(2-3) (2007) 131–139. https://doi.org/10.1016/j.ultramic.2006.06.008.

[26] R. Hu, S. Jin, G. Sha, Application of atom probe tomography in understanding high entropy alloys: 3D local chemical compositions in atomic scale analysis, Prog. Mater. Sci. 123 (2022) 100854. https://doi.org/10.1016/j.pmatsci.2021.100854.

[27] S.S. Kube, S. Sohn, D.Uhl, A. Datye, A. Mehta, J. Schroers, Phase selection motifs in High Entropy Alloys revealed through combinatorial methods: Large atomic size difference favors BCC over FCC, Acta Mat. 166 (2019) 677–686. https://doi.org/10.1016/j.actamat.2019.01.023.

[28] S. Ghosh, N. Ofori-Opoku, J. E. Guyer, Simulation and analysis of γ-Ni cellular growth during laser powder deposition of Ni-based superalloys, Comp.Mat. Sci. 144, (2018) 256–264, https://doi.org/10.1016/j.commatsci.2017.12.037.

[29] S.C. Flood, J.D. Hunt, Columnar and equiaxed growth I. A model of a columnar front with a temperature dependent velocity. J. Cryst. Growth, 82 (1987) 543–551. https://doi.org/10.1016/0022-0248(87)90346-0.

[30] D. Farkas, A. Caro. Model interatomic potentials for Fe–Ni–Cr–Co–Al high-entropy alloys. J. Mat. Res. 35.22 (2020) 3031–3040. https://doi.org/10.1557/jmr.2020.294.

[31] L. Zai, C. Zhang, Y. Wang, W. Guo, D. Wellmann, X. Tong, Y. Tian, Laser powder bed fusion of precipitation-hardened martensitic stainless steels: a review. Metals, 10(2), (2020) 255. https://doi.org/10.3390/met10020255.

[32] N. Haghdadi, M. Laleh, M. Moyle, S, Primig, Additive manufacturing of steels: a review of achievements and challenges. J. Mater. Sci. 56 (2021) 64–107. https://doi.org/10.1007/s10853-020-05109-0.

[33] R. Seede, B.Zhang, A. Whitt, S. Picak, S. Gibbons, P. Flater, A. Elwany, R. Arroyave, I.Karaman, Effect of heat treatments on the microstructure and mechanical properties of an ultra-high strength martensitic steel fabricated via laser powder bed fusion additive manufacturing. Addit. Manuf.47 (2021) 102255. https://doi.org/10.1016/j.addma.2021.102255.

[36] Z. Liu, Z. Xiong, K. Chen, X. Cheng, Mechanical properties of large-size $AlCoCrFeNi_{2.1}$ eutectic high-entropy alloy via hot-rolling followed by annealing, MEMAT 2022; 2nd International Conference on Mechanical Engineering, Intelligent Manufacturing and Automation Technology, (2022) *1–4*.

[37] A.W. Thompson, Substructure strengthening mechanisms. Metall. Mater. Trans. A 8, (1977) 833–842. https://doi.org/10.1007/BF02661564.

[38] H. E. Sabzi, E. Hernandez-Nava, X.-H. Li, H. Fu, D. San-Martín, P.E.J. Rivera-Díaz-del-Castillo, Strengthening control in laser powder bed fusion of austenitic stainless steels via grain boundary engineering, Mater. Des 212, (2021) 110246. https://doi.org/10.1016/j.matdes.2021.110246.

Tables

Table 1: LPBF processing parameters for dense samples (density >99.8%)

Preheating (°C)	Laser power (W)	Scanning velocity (mm/s)	Hatch spacing (µm)	Layer thickness (µm)
200°C	200-250	1000-1200	80	40

Table 2: Experimental composition of the hypoeutectic alloy (powder) by chemical analysis using ICP, LECO-IGR and LECO-CS compared to the nominal composition and the eutectic composition.

	Alloying elements (at.%)				Impurities by LECO-IGF, -CS (ppm)			
	Al	Cr	Fe	Ni	O	N	C	H
Experimental	15.4	19.6	20.9	44.1	150	30	81	6
Nominal	15.5	20.6	20.6	43.3	Not specified			
Eutectic	16.3	20.4	20.4	42.9	Not specified			

Table 3: Microstructure key figures from image analysis

Condition	Phase fractions, area%			Characteristic spacing, µm
	A1(FCC)	B2(BCC)	A2(BCC)	
LPBF as-built	85.6	14.4 (B2+A2)		Cellular spacing 0.52 ±0.13
Annealed 850°C/6h	59.9	29.3	10.8	Lamellar spacing 0.43 ±0.04
Annealed 950°C/6h	61.0	30.4	8.6	Lamellar spacing 0.67 ±0.05

Table 4: Mechanical properties obtained from micro-indentation and three-point bending

Test specimen condition	Micro-indentation	Flexural properties from three-point bending		
	Microhardness, (HV0.2)	$YS_{0.2\%}$, (MPa)	UTS , (MPa)	Elongation (%)
LPBF as-built	402 ± 8	1655 ± 160	2115 ± 40	17.8 ± 0.9
LPBF+ 850°C, 6h	437 ± 4	1570 ± 50	2206 ± 40	7.2 ± 0.7
LPBF+ 950°C, 6h	387 ± 5	1303 ± 21	2098 ± 13	11.3 ± 0.7
As-cast reference	310 ± 6	762± 15	1736 ± 23	13.6 ± 1.2

Table 5: Phase composition of different phases analyzed by APT in the as-built LPBF sample

Crystal structure	Element content (at.%)					
	Al	**Cr**	**Fe**	**Ni**	**Mn**	**Si**
A1(FCC)	14.95	21.36	21.83	41.75	0.07	0.04
B2(BCC)	30.64	5.76	10.62	52.88	0.06	0.04

B2(BCC)# spinodal	28.30	9.12	12.10	50.38	0.06	0.04
A2(BCC)# spinodal	4.50	52.52	30.30	12.58	0.06	0.04

Table 6: Phase composition of different phases analyzed by APT in the sample annealed at 950°C/6h.

Crystal structure	Element content, at.%					
	Al	**Cr**	**Fe**	**Ni**	**Mn**	**Si**
A1(FCC)	5.065	23.83	31.50	39.52	0.02	0.07
B2(BCC)	34.80	1.28	8.30	55.57	0.04	0.01
A2(BCC)	0.21	82.75	14.43	2.53	0.04	0.03

Declaration of interests

☒ The authors declare that they have no known competing financial interests or personal relationships that could have appeared to influence the work reported in this paper.

☐The authors declare the following financial interests/personal relationships which may be considered as potential competing interests: